Interferometric SAR MultiTemporal processing

(techniques and applications)

By D. Perissin

Introduction

Active radar imaging is a coherent technology that allows the generation of interferograms. An interferogram is the product of one image by the complex conjugate of another image. Whenever a correlation exists between corresponding pixels in the two images, the interferometric phase reveals very precise readings of the sensor-target distance. The phase is in fact a precise measurement of the alignment between two radar signals (as shown in Figure 1) which is a fraction of the wavelength. Since microwave signals have wavelength in the order of centimeters, the interferometric phase has the potential to read changes of distance with sub-millimeter precision.

The first Synthetic Aperture Radar Interferometry (InSAR) experiment was carried out by Graham in 1974 [1], using two receiving antennas mounted on an aircraft. In 1988 Goldstein published the first single-antenna repeat-pass InSAR Digital Elevation Map retrieved through interferometric processing of two images acquired by the Shuttle Imaging Radar (SIR-B) [2]. Even though the potential of InSAR was clear since the beginning, many were the limitations and difficulties related to the technology. Changes in the terrain reflectivity cause radar decorrelation, which makes the InSAR phase unreadable [3]. Moreover, atmospheric water vapor delays radar signals, turning phase readings into precise but inaccurate measurements [4]. It took a bit more than a decade before the availability of multi-temporal archives brought to the discovery of techniques for overcoming the InSAR limitations. Pioneer in multi-temporal InSAR processing is the Polytechnic of Milan, which published and patented the Permanent Scatterers technique (PSInSAR) in early 2000 [5]. Since then, many groups worldwide worked on different Multi-temporal InSAR approaches (also called PSI, Persistent Scatterer Interferometry). Picking up a few representatives, it is worth to quote the Small Baseline Subset (SBAS) InSAR [6], the Stanford Method for PSs (StaMPS) [7] up to the most recent SqueeSAR [8]. For a more complete list of references, the interested reader can refer to two recent reviews sketching the state of the art of SAR and multi-temporal InSAR [9], [10].

Applications of multi-temporal InSAR are mainly ground movements detection and DEM estimation. Examples of terrain movements are landslides [11], subsidence (natural or due to underground operations as mines, excavations, water/oil extraction) [12], soil compaction, seismic activity [13], volcanoes activity [14]. However, with appropriate techniques and with higher spatial resolution, multi-temporal InSAR can also be successfully exploited to monitor buildings and infrastructures. Many examples of InSAR DEM generation are available from the literature [15], and the most recent mission dedicated to this aim is the Tandem-X bistatic configuration [16]. Nevertheless, repeat-pass interferometry has been shown providing useful information also for terrain mapping and classification [17].

Several books have been published on Synthetic Aperture Radar, SAR Interferometry and related processing techniques. Among them, we wish to quote here Curlander for SAR [18], the European Space Agency (ESA) manual for InSAR [19] and Kampes for PSI [20]. It is not aim of this chapter to present a

complete review of all works carried out in this field, neither to cover all possible multi-temporal techniques. Rather, the attempt is to provide the reader with a set of concepts for understanding the basics of InSAR and to conduct him through a series of experiments to keep the discussion as applied as possible.

The author of this Chapter received his education at the Polytechnic of Milan, where he started researching on PSI. After a few years as a postdoc in the same institution, he moved to Hong Kong as research assistant professor at the Chinese University and he is currently with the Civil Engineering School at Purdue University as assistant professor. The examples reported in this chapter have been processed with the software Sarproz [21], [22] developed by the author in his 12 years research career. The interested reader may replicate the examples by requesting the author for a Sarproz license.

The present Chapter is divided into two sections. In the first section, the basic of SAR interferometry are introduced, starting from the definition of the geometry of the problem and ending up with phase unwrapping. The second section presents the main PSI concepts, together with a few more recent extensions of the original Permanent Scatterers ideas, like multi-master and weighted approaches and non-linear time series estimation.

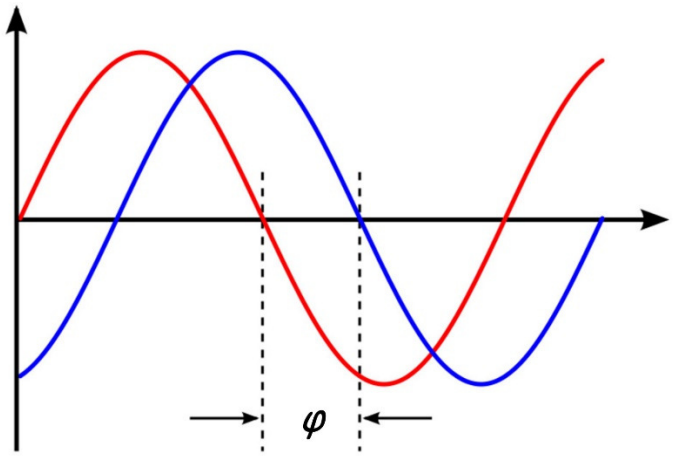

Figure 1. The phase difference φ quantifies the delay or misalignement between two ElectroMagnetic signals. Since microwaves are characterized by centimetric wavelengths, the phase can reveale millimiter changes.

SAR interferometry

For tackling InSAR concepts and processing techniques, we assume in this Chapter to deal with a set of co-registered SAR images. SAR images may be delivered by data providers either in L0 format (raw data) or in L1 format (also called SLC, Single Look Complex). Raw data need firstly to be focused before co-registration. The process of co-registration refers to the alignment of two SAR images, so that corresponding pixels in the two images contain the same portion of imaged terrain. To perform interferometry, images acquired with the same nominal geometry (orbit and incidence angle) are required. Even when the nominal geometry is the same, the satellite position may be slightly different from one acquisition to the other, and this is at the origin of the images misalignment. Usually, a single image is taken as reference (the Master image) and all other images (called Slaves) are resampled on the same sampling grid. We call pixel coordinates in range "samples" and pixels coordinates in azimuth "lines". We will not consider hereafter possible oversampling factors and we assume to deal with zero-doppler geometry[1] (even if both aspects could be modified without affecting significantly the treatment).

We call $Img_i(s,l)$ the complex value of image *i* at coordinates *s,l*. An example of intensity and phase of a SAR image is shown in Figure 2. Like all pictures presented in this Chapter, samples are the vertical coordinate (range) and lines the horizontal one (azimuth). The SAR image intensity in Figure 2 reveals three buildings (the image has been taken in Hong Kong on the 25th of October 2008 by TerraSAR-X). The picture of the phase looks simply noisy. This is due to the independency of the phase of nearby resolution cells. In fact, each resolution cell (corresponding to about 3m by 3m on the ground for TerraSAR-X) is plotted with a color showing the corresponding phase value ϕ. Assuming a single target is present in a resolution cell, the phase can be expressed as a function of its distance R_i from the sensor in the following way:

$$\phi_i = \frac{4\pi}{\lambda} R_i \qquad 1$$

The phase quantity in Eq. *1* is ambiguous and it is measured in radians, thus

$$\phi_i = \phi_i \pm 2n\pi \qquad 2$$

where *n* is an arbitrary integer number. For TerraSAR-X $\lambda = 3.1cm$. Considering that the target may be located anywhere in the resolution cell (3m by 3m), it becomes evident how the phase of two nearby resolution cells is totally independent. In case more targets would be present in the resolution cell, the discussion would be slightly more complex, but the outcome would not change.

The interference between two radar images removes the independent component of the phase, leaving just phase variations among nearby resolution cells, which may be correlated, as visible in Figure 3. The interferogram between images *i* and *k* can be expressed as

$$Int_{i,k}(s,l) = Img_i(s,l) \cdot Img_k^*(s,l) \qquad 3$$

In Eq. *3* the product is applied pixel by pixel and the star sign * indicates the complex conjugate. The interferometric phase between images *i* and *k* can be expressed as

$$\phi_{i,k}(s,l) = \phi_i(s,l) - \phi_k(s,l) \qquad 4$$

[1] In zero-doppler geometry, a target is focused at the location where it's closer to the satellite (as if the satellite would be looking down orthogonally to its path)

and by exploiting Eq. *1* we obtain:

$$\phi_{i,k}(s,l) = \frac{4\pi}{\lambda}\left[R_i(s,l) - R_k(s,l)\right] \qquad 5$$

Figure 3 shows an example of interferogram generated between the image in Figure 2 and the Master image acquired in November 2009. While the phase of the image in Figure 2 was totally uncorrelated, the interferogram shows correlation on the facades of the three imaged buildings.

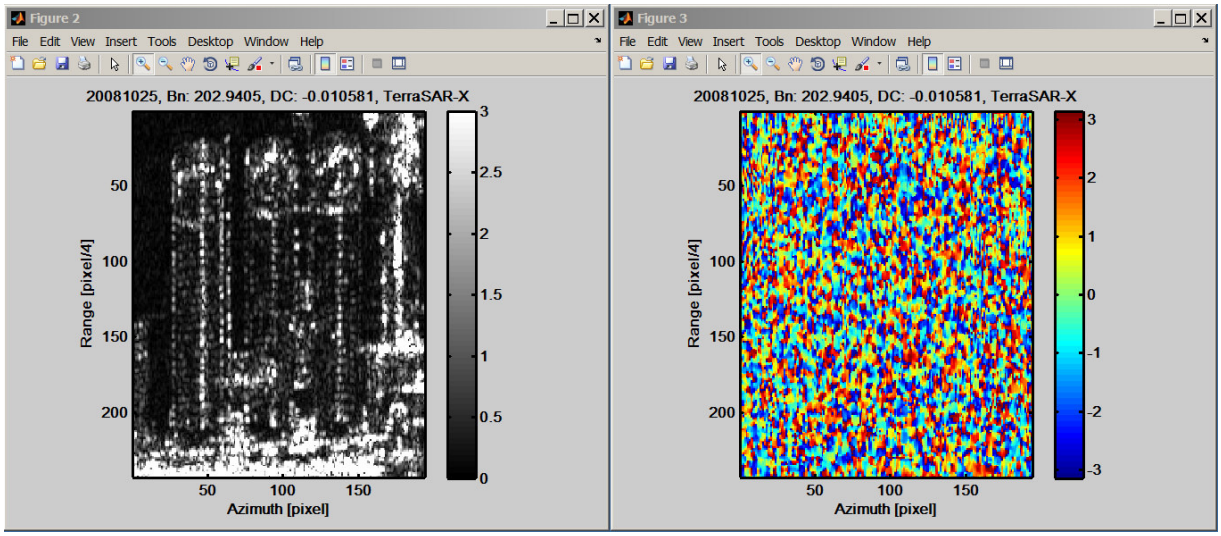

Figure 2. Intensity (left) and phase (right) of a complex SAR image taken in Hong Kong by TerraSAR-X on 25th of October 2008. Three buildings are visible.

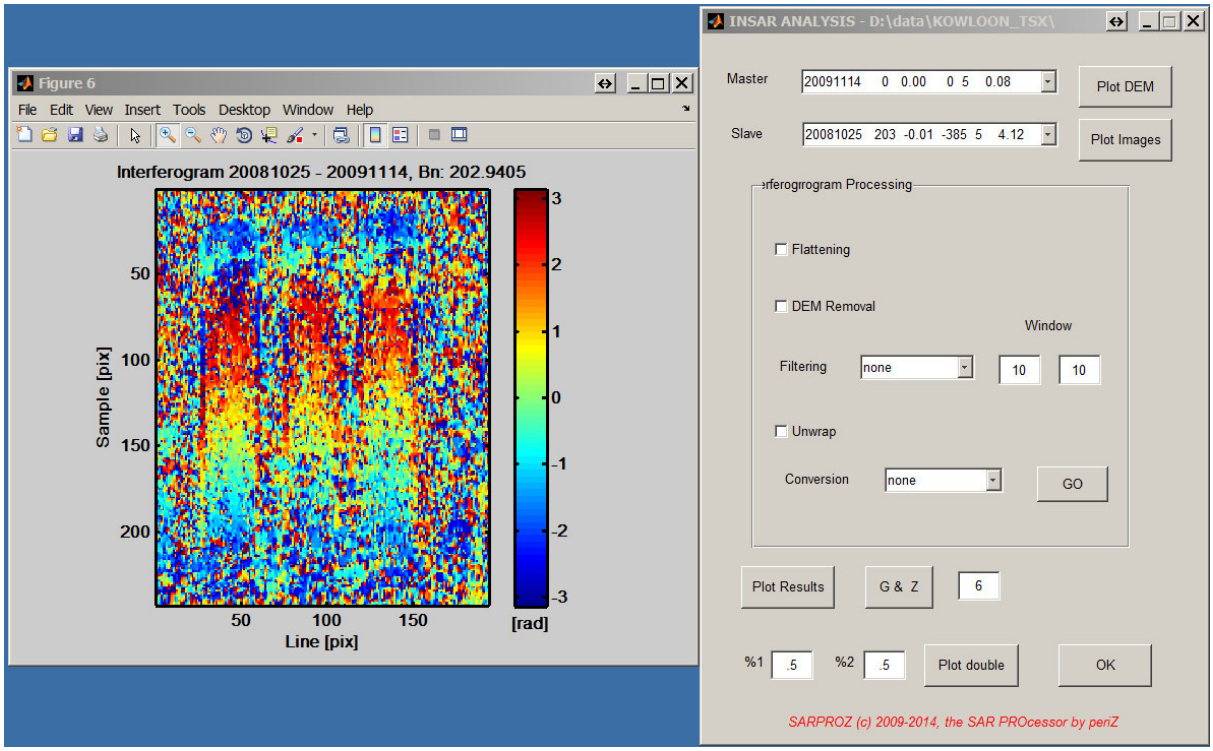

Figure 3. Example of interferogram generated between the image shown in the previous picture and the Master image (taken on the 14th of November 2009). On the right the Sarproz window used for interferogram generation is shown.

The InSAR Geometry

In order to better understand the interferometric phase in Equation *5*, we refer to the geometry depicted in Figure 4. We abandon for a moment the pixel notation *s,l* and we concentrate on the targets coordinates on the ground. We want to derive the interferometric phase at point *P* with respect to a reference point *O*. Point *P* lies at a distance Δ*x* from *O* and at a height Δ*h*. The satellite reference location (Master) is S_k, while the Slave position is S_i. The relative position between Master and Slave is measured in terms of distance along the direction normal to the reference slant range (indicated with *r* in Figure 4), and it is called Normal Baseline B_n. The relative incidence angle $\Delta\theta$ is thus

$$\Delta\theta = \frac{B_n}{R_k} \tag{6}$$

where $R_k = \overline{S_k O}$ is the Master range of reference point *O*. The relative interferometric phase is thus

$$\Delta\phi_{i,k} = \phi_{i,k}(P) - \phi_{i,k}(O) = \frac{4\pi}{\lambda}\left[R_{i,k}(P) - R_{i,k}(O)\right] \tag{7}$$

where $R_{i,k}(P) = \overline{S_i P} - \overline{S_k P}$ and $R_{i,k}(O) = \overline{S_i O} - \overline{S_k O}$. The double difference operation can be solved via trigonometry, leading to the following expression:

$$\Delta\phi_{i,k} = \frac{4\pi}{\lambda}\frac{B_n}{R_k}\left|\overline{OP}\right|_n \tag{8}$$

where $\left|\overline{OP}\right|_n$ (the blue arrow in Figure 4) is the projection of $\overline{OP}$ onto the direction normal to *r*. The term can be further decomposed into slant range and height components

$$\left|\overline{OP}\right|_n = \frac{\Delta r}{\tan\theta} + \frac{\Delta h}{\sin\theta} \tag{9}$$

as easily derived by looking at Figure 4 on the right.

By combining Equations 8 and 9 the relative interferometric phase becomes

$$\Delta\phi_{i,k} = \Delta\phi_{i,k}^{flat} + \Delta\phi_{i,k}^{height} \tag{10}$$

where

$$\Delta\phi_{i,k}^{flat} = \frac{4\pi}{\lambda}\frac{B_n}{R_k}\frac{\Delta r}{\tan\theta} \text{ and } \Delta\phi_{i,k}^{height} = \frac{4\pi}{\lambda}\frac{B_n}{R_k}\frac{\Delta h}{\sin\theta} \tag{11}$$

are called respectively flat terrain and topographic (height) phase terms.

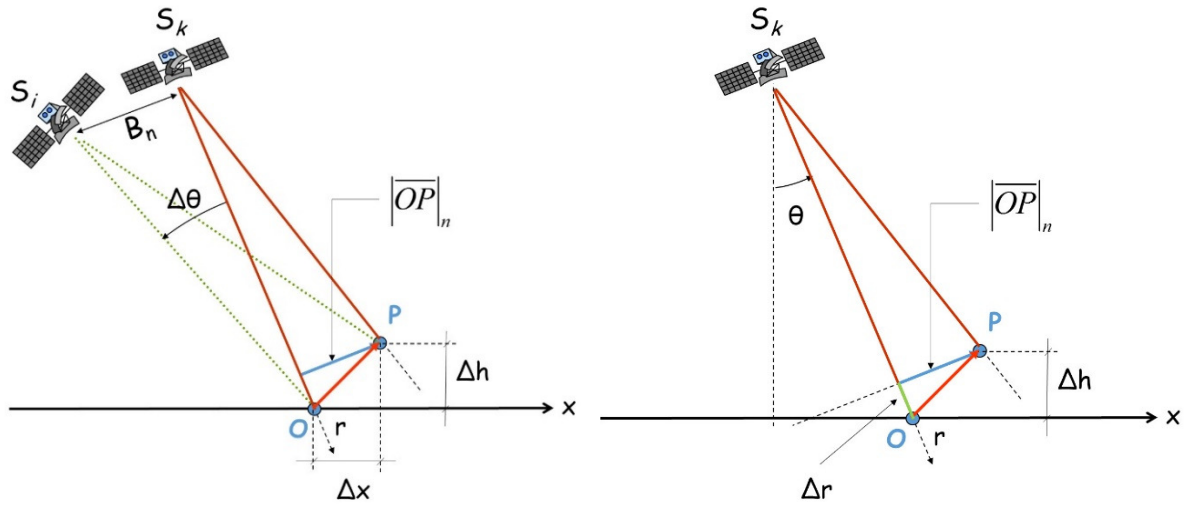

Figure 4. Acquisition geometry for interferogram generation. S is the satellite at positions i and k. O is the reference point and P the target under examination. P is located at distance Δx w.r.t. O and at height Δh. The Master slant range is indicated as r. On the right the projections of OP along slant range and cross-range (normal to slant range) are highlighted in green and blue respectively.

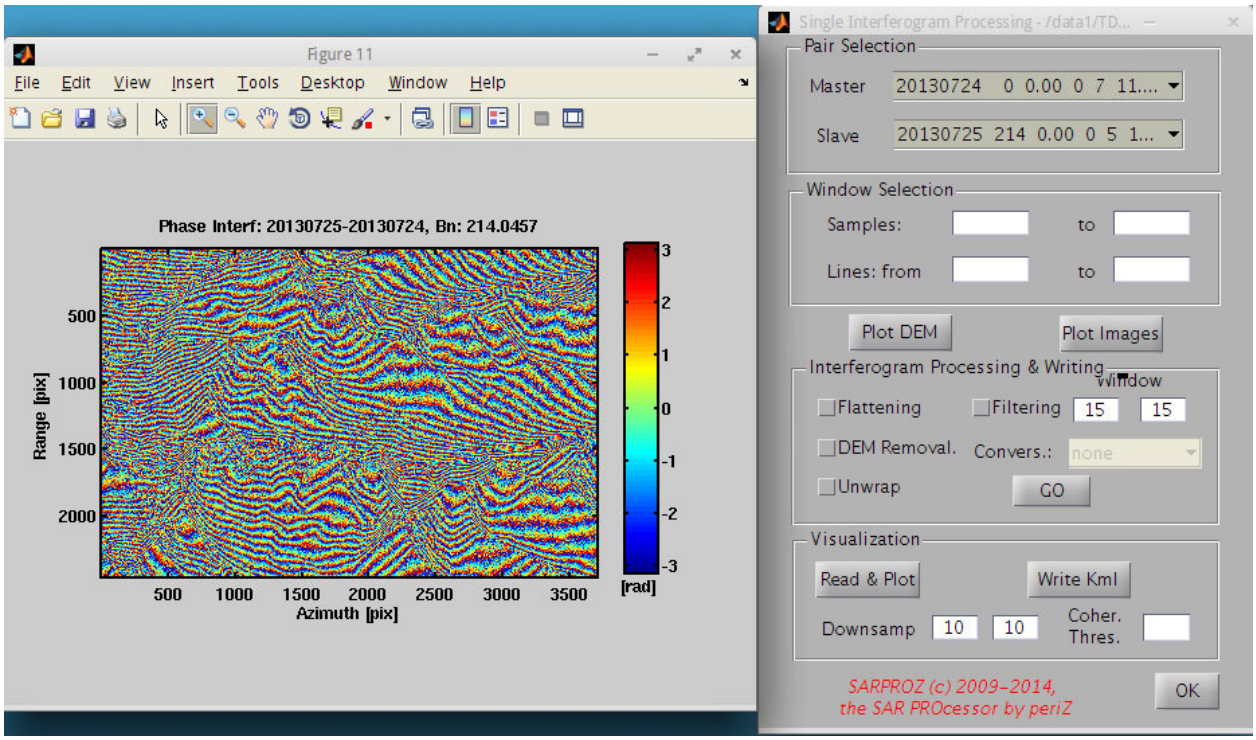

Figure 5. Example of Tandem-X interferogram (Normal Baseline =214m). Fringes in the range direction (vertical in the image) show the flat terrain phase component

Interferogram flattening

Equations 10 and 11 highlight the first two main components of the interferometric phase. The first of them, the flat terrain phase term, is depending on the slant range coordinate of target *P* (and not on its height). In a generic interferogram $Int_{i,k}(s,l)$ we can thus expect a phase ramp in range direction, function of the coordinate *s*, with a rate proportional to the interferometric baseline B_n. An example of flat terrain phase component is shown in Figure 5, where a Tandem-X interferogram is reported. The Interferometric baseline B_n is equal to 214m. A longer baseline would generate a higher frequency of fringes.

The flat terrain phase term is not carrying information useful for any kind of applications and it is usually simply removed. However, in case orbital data are not available, the flat terrain phase ramp can be used to estimate the interferometric normal baseline. The aim can be easily reached via a Fourier transform in the two-dimensional space range/azimuth. Conversely, if orbital data are available, the flat terrain phase term can be estimated by simulating the interferometric phase generated by a surface in ground coordinates with constant ellipsoidal height.

Figure 6 shows an example of flattened interferogram (that is, after removing the flat terrain phase term). The area reported in Figure 6 is the same as the one in Figure 5, the difference between the two images is the flat terrain removal.

The topographic term

The second phase term in Equations *10* and *11* is proportional to the height of point *P* with respect to the reference point *O*. This phase component reveals that interferograms are sensitive to the topography of the observed area. This is the reason why the production of Digital Elevation Maps (DEM's) was the first application developed for SAR interferometry over land.

From Equation *11* we can derive an important quantification of the sensitivity of the interferometric phase towards topography: the ambiguity height. The ambiguity height Δh_a is the height that generates a phase rotation equal to 2π.

$$\Delta h_a = \frac{\lambda R_k \sin\theta}{2B_n} \qquad 12$$

In other words, while looking at a flattened interferogram like the one shown in Figure 6, each phase fringe corresponds to a height range Δh_a. It is easy to understand then that the integration of all phase fringes in a flattened interferogram would lead to the estimation of the topography of the observed area. The operation of integration of phase fringes, when possible, is called phase unwrapping, and it will be discussed later in this Section.

Equation *11* shows the role played by the interferometric baseline B_n in the height estimation. A large normal baseline reduces the ambiguity height, increasing the frequency of topographic fringes of a given area. While this could be desirable for achieving a higher sensitivity of the interferometric phase towards the terrain height, its drawback is to cause decorrelation of the interferometric phase. Also decorrelation will be addressed further in this Section.

Other geometrical InSAR phase components may arise as a consequence of variation of other acquisition parameters (like central frequency and Doppler Centroid). Moreover, a precise treatment should consider the possible presence of single strong scatterers in the resolution cell and their sub-cell location. For both topics, the interested reader can refer to [23],[24] for a detailed analysis.

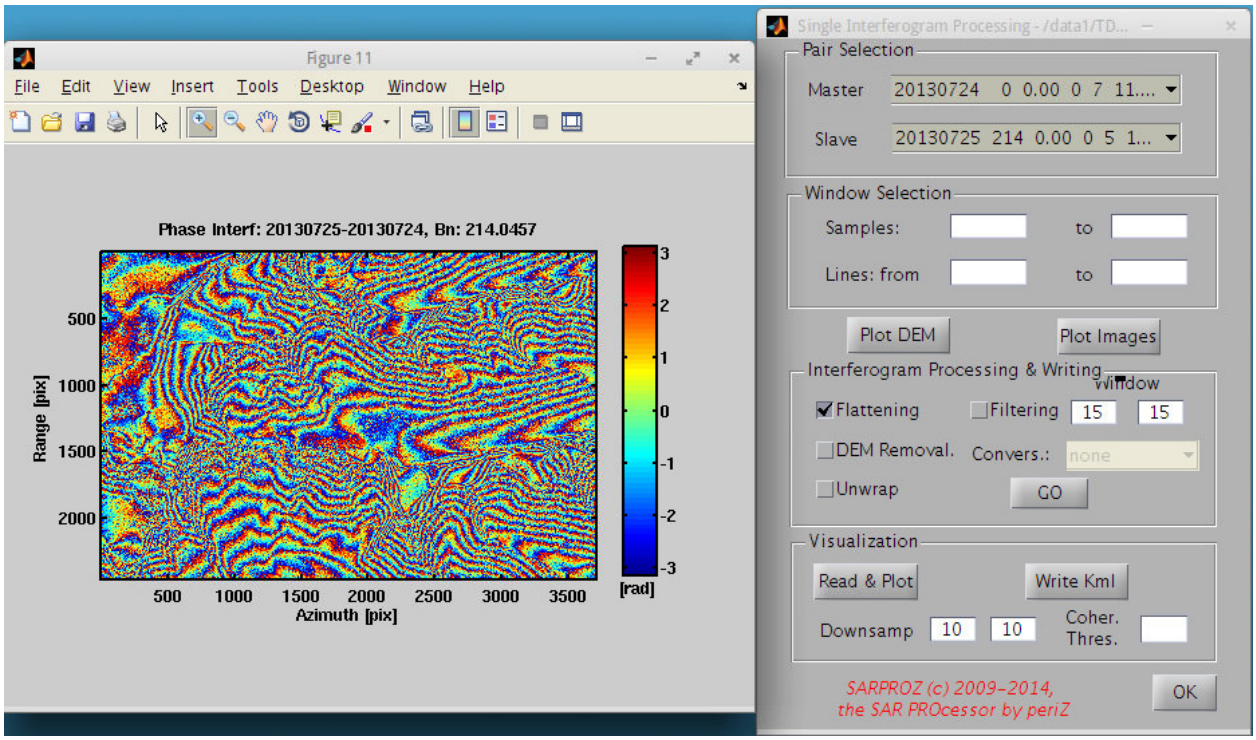

Figure 6. Example of Tandem-X interferogram (Normal Baseline =214m), after estimation and removal of the flat terrain. Fringes are proportional to the topography of the imaged terrain.

Differential interferometry and displacement detection

Repeat pass SAR interferometry is possible thanks to the characteristics of the orbits along which SAR satellites fly. Satellites carrying SAR sensors for Earth Observation are usually placed along sun-synchronous Polar orbits, which allow scanning the Earth surface regularly with a given (usually fixed) revisit time. In particular, every time a satellite flies over a given point on the ground at each revisit time, the UTC time of the day is the same, allowing keeping environmental parameters with daily variations constant. Moreover, the orbital tubes are designed in order to guarantee a distribution of normal baseline values compatible with interferometry.

As a consequence, besides the geometric component discussed in the previous sections, the interferometric phase may be influenced by the terrain displacement occurred between the two acquisition times. A movement of point *P* in a generic direction can be expressed in the *x,h* plane as

$$\vec{d} = \delta\vec{x} + \delta\vec{h} \qquad 13$$

where the arrow indicates a vector. The range displacement detected by the radar would therefore be

$$\Delta\phi_{i,k}^{disp} = \frac{4\pi}{\lambda}\left|\vec{d}\right|_r = \left|\delta\vec{x}\right|\sin\theta + \left|\delta\vec{h}\right|\cos\theta \qquad 14$$

The interferometric phase is thus very sensitive to displacement (half a wavelength movement causes a 2π phase rotation). However, the sensitivity is only along the slant range *r*. Given a single acquisition geometry, it is not possible to reconstruct the direction of the displacement. Moreover, a movement in the direction orthogonal to the slant range would not be detected at all. For an incidence angle ϑ=30deg, almost 90% of the vertical component of the displacement would be detected by the sensor, against only 50% of the horizontal component.

The high sensitivity to displacement is what makes InSAR a very powerful tool for detecting ground movements. Whenever displacement estimation is the aim of the interferometric analysis (rather than topographic reconstruction), it is therefore helpful to remove the geometric phase component to facilitate the identification of phase temporal changes. The interferometric phase after removal of flat terrain and topographic phase components is called Differential Interferometric phase (DInSAR):

$$\Delta\phi_{i,k}^{DInSAR} = \Delta\phi_{i,k} - \Delta\phi_{i,k}^{flat} - \Delta\phi_{i,k}^{height} \qquad 15$$

An example of Differential interferogram is shown in Figure 7. The interferogram in Figure 7 has been generated using a pair of Envisat images over L'Aquila acquired one before and one after the Earthquake happened in 2009. To remove the topographic phase component SRTM data was used.

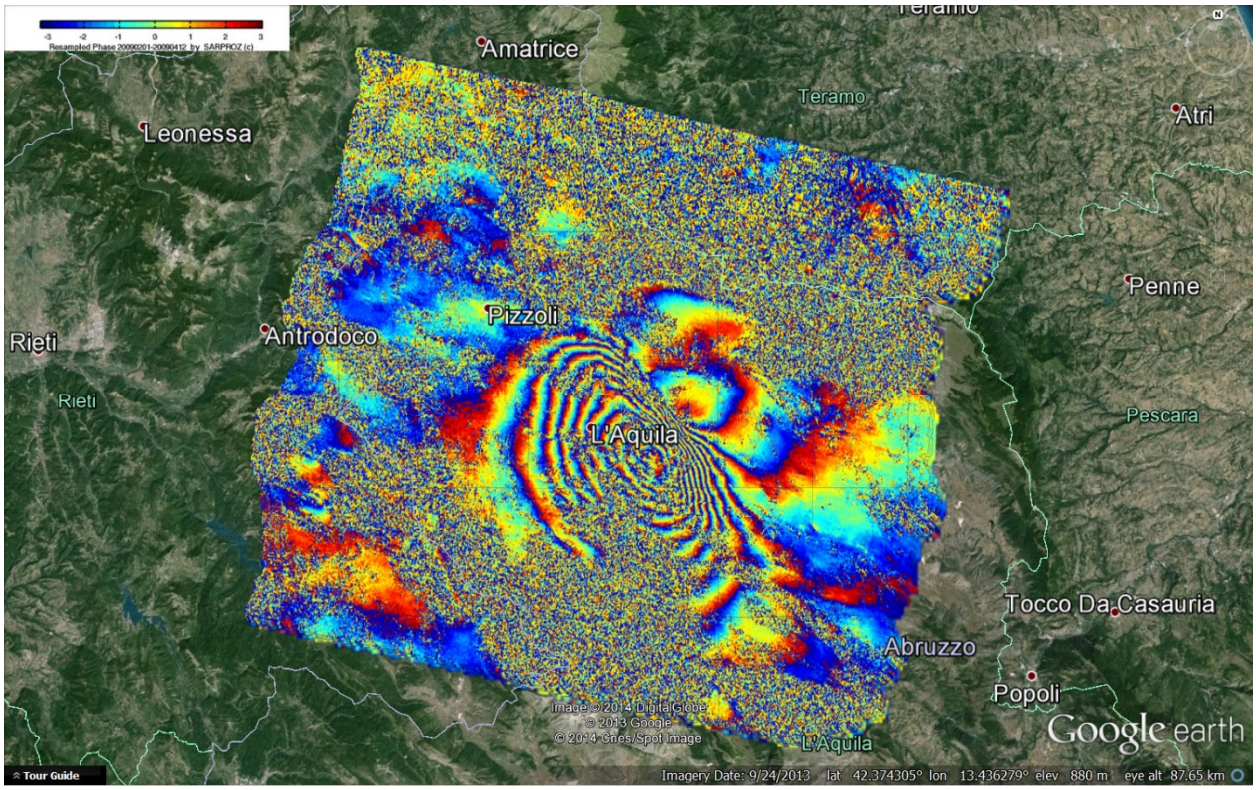

Figure 7. Example of geocoded Differential Interferogram produced by Sarproz using Envisat images (20090201-20090412) showing the displacement caused by L'Aquila Earthquake. SRTM data has been used to remove the topographic phase component. (processing by A. Rocca)

Phase decorrelation and the interferometric coherence

InSAR is potentially an extremely powerful technique for DEM generation and displacement monitoring. However, whenever changes occur in the terrain reflectivity, the two images involved in the interferogram generation may lose correlation and the phase may become unreadable. An example of this can be observed in Figure 7, where the fringes become noisy. Changes could occur in time: some terrain characteristic (like shape, material, orientation) is modified. This happens often e.g. in case of vegetation/forests/fields, but also in case of human activities. We talk therefore of temporal decorrelation. However, changes could occur also because of geometric modification of the terrain reflectivity: due to the short wavelength of the radar signal, even slight changes of the looking angle may determine very different reflections [24]. This phenomenon takes the name of geometric decorrelation.

Regardless the source of decorrelation, it is useful to quantify its impact. To this aim, the normalized complex cross-correlation coefficient of images *i,k* is used:

$$\gamma_{i,k} = \frac{E\left[Img_i Img_k^*\right]}{\sqrt{E\left[\left|Img_i\right|^2\right]}\sqrt{E\left[\left|Img_k\right|^2\right]}} \qquad 16$$

In Equation *16* $E[\ ]$ denotes the expected value. The absolute value of $\gamma_{i,k}$ is called interferometric coherence. Values of the coherence close to 1 indicate high correlation between the two images, and thus readable interferometric phase. Conversely, low coherence identifies decorrelation and thus noisy and unreliable phase.

In order to estimate the quantity in Equation *16* two main aspects have to be addressed. The first one is the substitution of the expected value with a spatial average of nearby pixels. Key role is played in this regard by size and shape of the window chosen for the average calculation. In the following we will simply adopt a general rectangular window, however, optimum performances are reached by an adaptive window. The second matter is phase ramps correction before the estimation of the expected value. Should the interferogram at the numerator of Equation *16* be taken raw, phase ramps caused e.g. by the flat terrain would strongly reduce the estimated coherence. The estimator of $\gamma_{i,k}$ can then be expressed as

$$\gamma_{i,k}(s,l) \cong \frac{\sum_{u,v \in Win(s,l)} Img_i(u,v) Img_k^*(u,v) e^{-j\Delta\phi_{i,k}^{model}(u,v)}}{\sqrt{\sum_{u,v \in Win(s,l)} \left|Img_i(u,v)\right|^2} \sqrt{\sum_{u,v \in Win(s,l)} \left|Img_k(u,v)\right|^2}} \qquad 17$$

The quantity $\gamma_{i,k}$ is calculated for each pixel *s,l* over a given window *Win(s,l)*. The term $\Delta\phi_{i,k}^{model}$ indicates the phase ramps to be removed and it may include one or more geometrical phase terms described in the previous paragraphs.

The interferometric coherence $\left|\gamma_{i,k}\right|$ is not only a useful indicator of the reliability of the interferometric phase. The coherence can be used also for change detection or classification purposes. An example is shown in Figure 8, where a case study in Italy, Mt Vesuvius is reported. The image on the left shows the

reflectivity map of the volcano. The image on the right is the interferometric coherence (in particular, the map displayed in Figure 8 has been generated from the average of 30 interferograms). It is very nice to notice the lava flows on the right and on the left of the caldera: they are pretty well visible from the coherence map, but not from the reflectivity map. The reason for the higher coherence is the lack of vegetation over the lava flows. The coherence can thus be used for mapping purposes, together with other SAR/InSAR products as well as with other data (as optical, multispectral, and more).

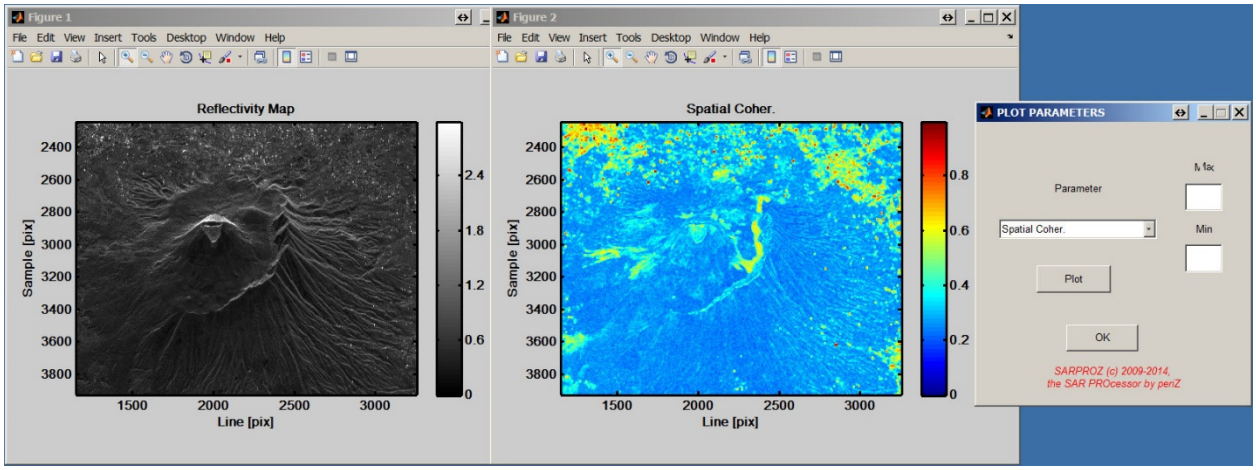

Figure 8. Mount Vesuvius, Italy. Left: reflectivity map. Right: spatial interferometric coherence (taken from the average of 40 interferograms). The coherence maps reveals lava flows on the right and on the left of the caldera. Lava flows are more coherent than the surrounding terrain because of the lack of vegetation.

Interferogram filtering

The absolute value of $\gamma_{i,k}$ tells us the correlation of nearby pixels. Its phase, on the other side, is an estimator of the expected value of the interferometric phase. The averaging operation of nearby pixels has the effect of smoothing noisy phase variations, enhancing the signal to noise ratio. This effect corresponds to the one of filtering for noise reduction.

Many typologies of filters have been introduced in the literature, addressing different aspects of decorrelation and of the possibility to recover information from noisy interferograms. Some of them are discussed in the ESA manual [19]. It is worth to mention here the most widely used InSAR filter, proposed firstly by Goldstein [25] and then later modified by other authors [26].

An example of interferogram filtered by the modified Goldstein filter is shown in Figure 9. The interferogram reported there is the same of Figure 6, and data have been taken by Tandem-X in bistatic configuration. After filtering, fringes are much cleaner, even if one can observe a few spots of decorrelation, in particular on the top of slopes.

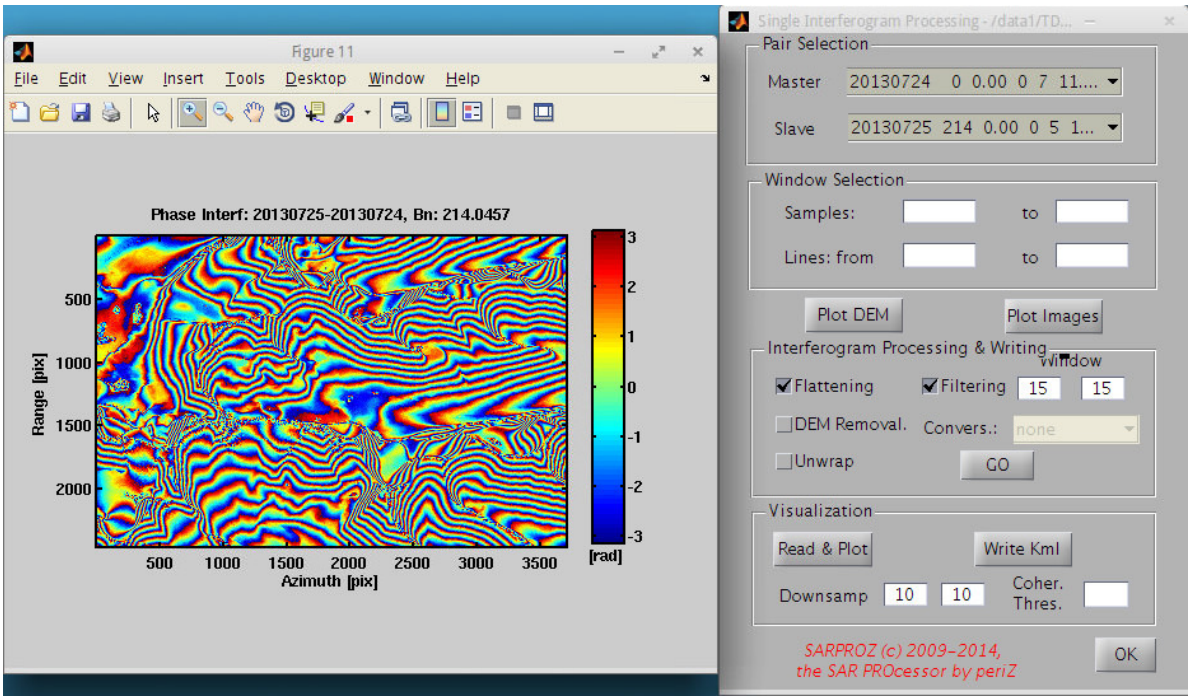

Figure 9. Filtered Tandem-X interferogram (the same area as in Figure 6). After filtering, fringes became much clearer, even if some spots of decorrelation can still be observed (in particular at the top of slopes).

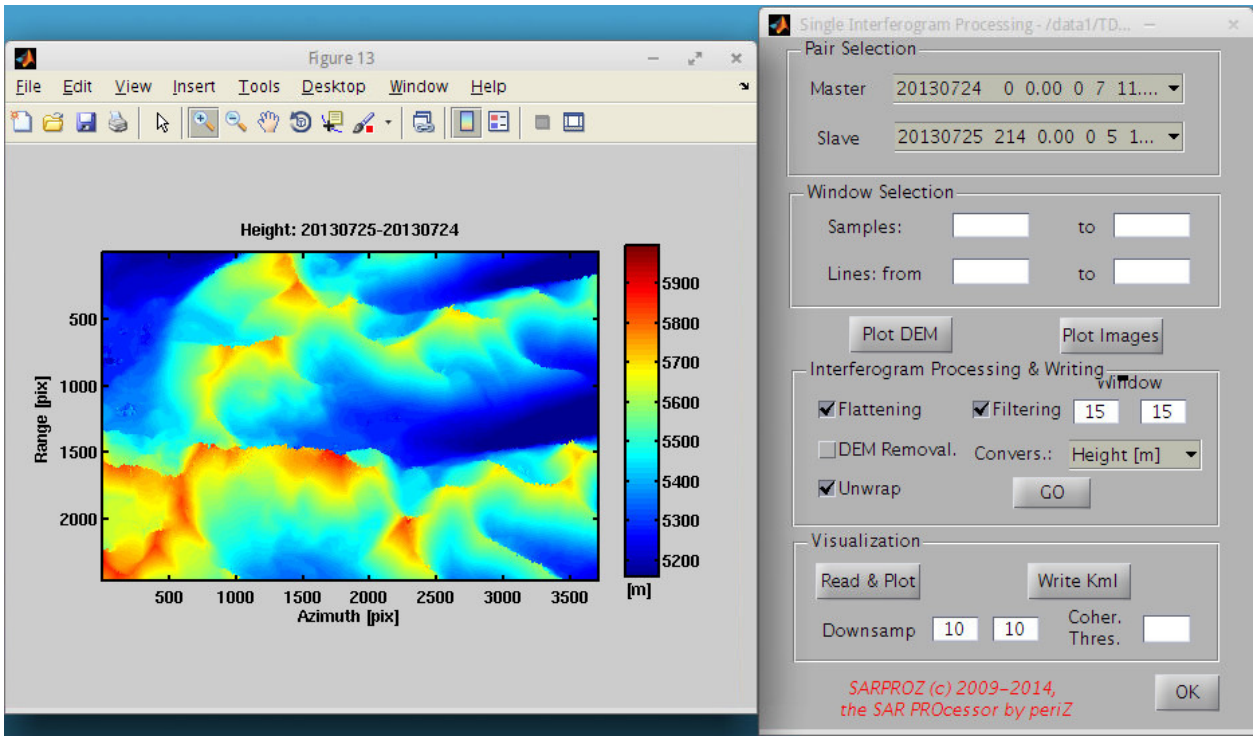

Figure 10. Unwrapped and converted interferogram. The Tandem-X interferogram previously shown has been here unwrapped and converted into meters. The high coherence allowed a very precise unwrapping. Some flickering noise is still present in low coherence spots.

Interferogram unwrapping

The integration of fringes of an interferogram for solving phase ambiguities is called phase unwrapping. More specifically, phase unwrapping refers to solving the following equation for the integer number *n*

$$\phi_{i,k}^{UW}(s,l) = \phi_{i,k}(s,l) \pm 2n\pi \qquad 18$$

The unwrapped phase (left in Equation *18*) is equal to the wrapped phase plus an integer multiple of 2π's. Usually, if an interferogram is highly coherent, phase unwrapping is not a big issue. However, in case of poor coherence it may even be impossible to solve Equation *18*. Or at least, it may be impossible to solve it using a single interferogram. We will see in the next Section how multi-temporal InSAR is actually a much more robust solution to phase unwrapping.

Several solutions have been proposed in the literature for the phase unwrapping problem. Also in this case, the ESA manual can furnish an overview of some of them, providing a good starting point for a deeper investigation of the topic [19].

An example of interferogram unwrapped by Sarproz is shown in Figure 10. The phase of the interferogram of Figure 9 has been unwrapped and converted into height. The final result is pretty nice and smooth, thanks to the high coherence of the Tandem-X interferogram. However, the low coherence spots are still visible in the unwrapped phase.

The atmospheric delay

Despite the high potential of SAR interferometry, even when high coherence is found and fringes unwrapped correctly, an attentive analysis trying to interpret the result in terms of topography or of terrain displacement may end up showing poor accuracy. The reason for the possible frustrating outcome is that repeat-pass SAR interferometry is affected by different atmospheric conditions at the acquisition time. Water vapor is in fact delaying radar signals and its spatially varying distribution biases the InSAR phase. Therefore, the expected millimeter precision of displacement measurements turns into centimeters accuracy, while the metric precision in height estimation can quickly become tens of meters.

In recent years many research group have worked on the atmospheric delay correction in InSAR [27]. Spectrometers, numerical weather models, GPS networks can in fact provide water vapor maps and partly mitigate atmospheric effects in InSAR, however, only at very low resolution and for very long spatial wavelengths. As a matter of fact, classical InSAR is strongly impaired by atmospheric disturbances. Research-based large scale applications (as earthquake modeling) are still possible, but, with a level of details far away from the claimed millimeter accuracy.

Figure 11 brings an example of the Atmospheric Phase Screen estimated by Sarproz. The dataset used in the analysis is composed by 64 TerraSAR-X images over Los Angeles. The footprint is 30km by 60km. From Figure 11 one can appreciate how important the impact of atmospheric delay is in X-band.

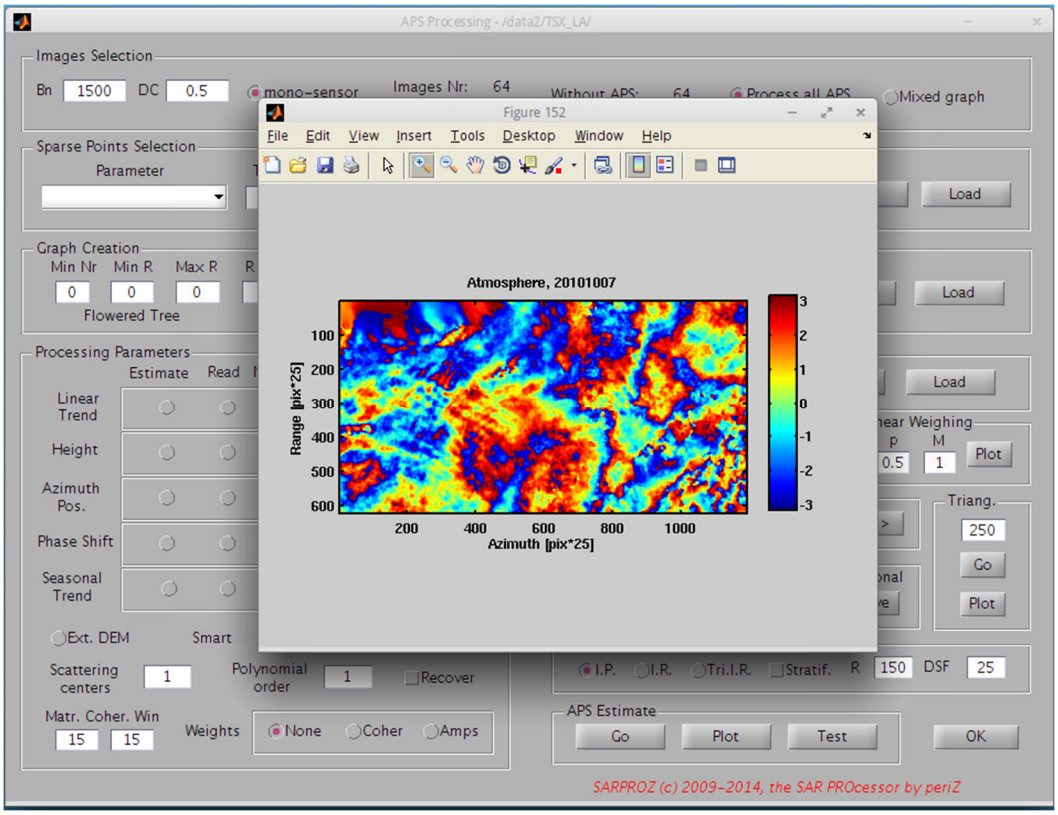

Figure 11. Example of atmospheric delay estimated from TerraSAR data over Los Angeles. The image is 30km by 60km wide, and the high atmospheric variability is revealed by the X-band short wavelength. In the background the Sarproz module for atmospheric delay estimation.

Multi-Temporal InSAR

In the previous Section we have introduced the basics of classic InSAR. SAR interferometry is a very promising technology, however, it is affected by a series of important problems. First of all, interferograms suffer decorrelation (temporal and/or geometrical). In second instance, the interferometric phase is wrapped, and it may be quite difficult (if possible at all) to unwrap it correctly using a single interferogram. Moreover, if the topography of the area of interest is not known with enough precision, it may be very hard to distinguish between residual topography and terrain displacement. Finally, even by solving all previous problems, atmospheric artefacts can vanish all efforts, strongly biasing the detected signals. In this section, we introduce a possible solution to the mentioned problems: Multi-Temporal InSAR.

Introduction

The first satellite carrying a SAR sensor for Earth Observation was the NASA Seasat in 1978. Even though its life time was quite limited, the mission was very useful to demonstrate the SAR capabilities. However, only with the launch of ERS-1 in 1991, archives of repeated SAR images became available. As soon as multiple images of the same area were collected, researchers started working at problems like DEM estimation via Multi-Temporal InSAR, trying to solve limitations as decorrelation, phase unwrapping, atmospheric delay. In early 2000, the Polytechnic of Milan firstly proposed the Permanent Scatterers (PS) technique [5]. The PS technique is based on the idea that, exploiting long series of SAR images, it is possible to identify targets that do not change their electromagnetic signature throughout the dataset. Such targets are not affected by temporal or geometrical decorrelation and their InSAR phase can thus be studied as a function of the acquisition parameters (normal and temporal baseline). It is possible then to observe that height, displacement and atmospheric delay show different spectral characteristics as a function of normal and temporal baseline and as a function of space. Based on such observation, their separation and estimation become then possible.

In this Section we will firstly introduce the basics of Persistent Scatterers Interferometry (PSI). Afterwards, we will discuss a series of extensions of the original ideas (like seasonal and non-linear signals estimation). We will then conclude the treatment with multi-master and weighted approaches. All examples brought here were processed by Sarproz [21],[22].

The PSI approach

To introduce here the main concepts of the PSI technology, we take our steps from a real processing example. The interested reader can replicate the experiment on its own using a licensed copy of Sarproz [21],[22]. The dataset under study is composed by N_I=51 TerraSAR-X images acquired over Hong Kong in the period October 2008 – May 2011. A sketch of the acquisition parameters of the dataset is reported in Figure 12. From the upper left corner of Figure 12 on the left, in clockwise order, we have the histogram of the Normal Baselines, the histogram of the Doppler Centroids, the temperature at the acquisition time, and the sensors that acquired the data (TerraSAR and Tandem). On the right of Figure 12 we can see the interferometric configuration of the analysis: each image is connected to form an interferogram with the Master image, chosen at the barycenter of the distribution of normal and temporal baselines. From Figure 12 on the right it is possible to observe 8 images with a lower barycenter of normal baselines: they are the 8 Tandem images of the dataset. The analyzed area is the same of the SAR image example reported in Figure 2, and it covers 3 buildings in the Hong Kong harbor.

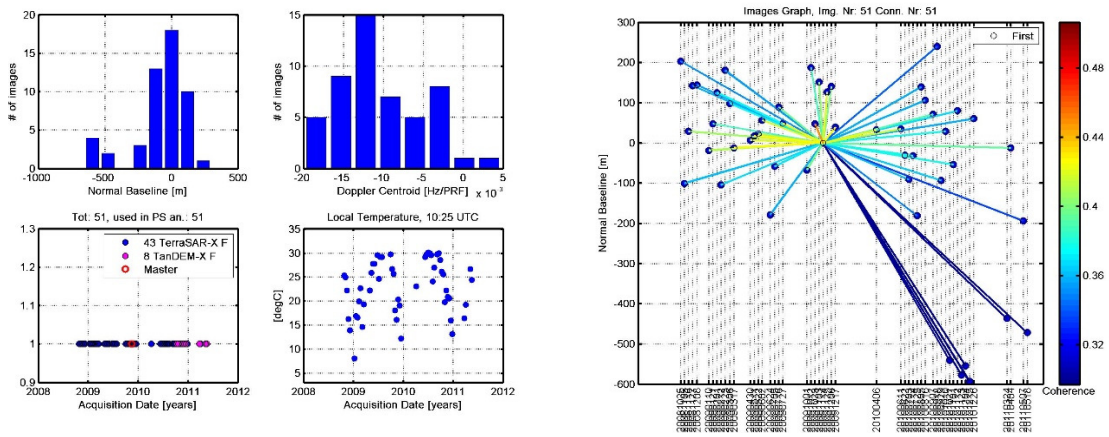

Figure 12. Dataset used in the PSI experiment. 51 images taken by TerraSAR-X in Hong Kong. On the left, upper plots: histograms of Normal Baseline and Doppler Centroid. Lower part, acquisition dates and temperature at the acquisition time. The image on the right shows the interferometric combination: one image is taken as reference and interferograms are generated with respect to it.

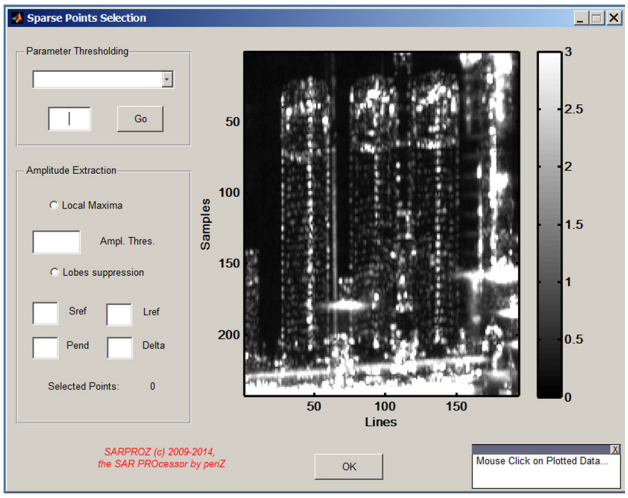

Figure 13 Reflectivity map (average intensity) of the area of interest. Three buildings are visible in the area of interest.

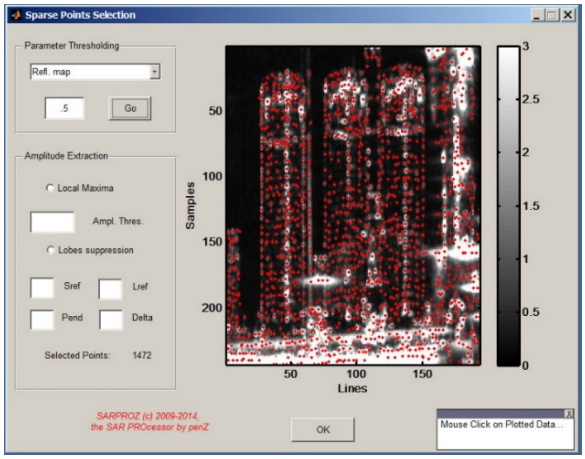

Figure 14. Targets selected for the PSI processing: 1472 points with Reflectivity higher than 0.5.

Figure 13 shows the starting point of the PSI analysis: the Reflectivity Map of the area of interest. The Reflectivity Map has been estimated as the average of all images of the dataset. It is interesting to compare it with the intensity of one single SAR image (as the one shown in Figure 2). The averaging operation has strongly suppressed the noise, enhancing all targets which kept stable reflectivity throughout the dataset.

We decide then to analyze all targets that present a visible peak in the image, and we select them posing a threshold on the Reflectivity equal to 0.5. Figure 14 shows N_p=1472 points selected for the analysis.

As previously mentioned, the aim of the analysis is solving the InSAR limitations, estimating height and displacement of targets. We take a reference point *o* among the selected targets (e.g. the one with highest Reflectivity) and we analyze the interferometric phase of all selected points *p* (we omit from now on the reference index *o* to lighten the notation)

$$\Delta\phi_{i,k}(p) = \Delta\phi_{i,k}^{flat}(p) + \Delta\phi_{i,k}^{height}(p) + \Delta\phi_{i,k}^{disp}(p) + \Delta\phi_{i,k}^{atmo}(p) + \Delta\eta_{i,k}(p) \qquad 19$$

Indexes *i,k* denote again the interferometric couple, with *k* master image and *i* a generic image of the dataset.

The interferometric phase in Equation *19* is made of the following components: flat terrain, height, possible displacement, atmospheric delay and noise. As stated in the previous Section, more factors should be considered for a complete analysis [23], [24], but we will keep the complexity limited in this discussion.

The first term in Equation *19*, the flat terrain, can be estimated from orbital data and removed. We will not consider here possible orbital inaccuracies for the sake of simplicity. The second term, the topographic phase, is given by Equation *11*, and it is linear with the normal baseline and with the target height. We can rewrite it here, making explicit the dependency of the height $\Delta h(p)$ on the target of interest *p* and the dependency of the normal baseline $B_{n,i}$ on the *i*-th image of the dataset:

$$\Delta\phi_{i,k}^{height}(p) = \frac{4\pi}{\lambda}\frac{B_{n,i}}{R_k}\frac{\Delta h(p)}{\sin\theta} \qquad 20$$

The third term is the displacement. A common way to model the displacement is that of assuming it linear in time. We will see later on in this Section that such assumption is not always working, but we take it as a starting point. Defining thus $\Delta v(p)$ the relative velocity of point *p* with respect to the reference and $B_{t,i}$ the temporal baseline

$$\Delta\phi_{i,k}^{disp}(p) = \frac{4\pi}{\lambda}\Delta v(p) B_{t,i} \qquad 21$$

The fourth term is the atmospheric delay. It has been shown in the literature that the atmospheric delay has a decorrelation length of several hundreds of meters [4]. We can thus assume its impact small in our area of interest, and neglect it. We will not consider here how to extend the analysis at bigger areas and estimate the Atmospheric Phase Screen. For that purpose, the interested reader can refer to [20].

The last term in Equation *19* is $\Delta\eta_{i,k}(p)$, with which we have indicated noise. The noise will be estimated from the model residuals, and it will tell us the stability and reliability of the target at hand.

As a conclusion, in our small area of interest, we can see our problem as a set of N_p equations with N_I samples each, where the unknowns are height $\Delta h(p)$ and velocity $\Delta v(p)$ of each point to be estimated in the space $B_{t,i}$-$B_{n,i}$. The system looks linear, but, considering that the phase is wrapped, it is not. In [5] the proposed solution to solve the system comes from the maximization of the periodogram in which height and velocity represent the 2-dimensional frequencies to be scanned. In formulas, the periodogram $\xi[\Delta v(p), \Delta h(p)]$ is

$$\xi[\Delta v(p), \Delta h(p)] = \frac{1}{N_I}\sum_{i=1}^{N_I} e^{j\left[\Delta\phi_{i,k}(p) - \kappa_v \Delta v(p) B_{t,i} - \kappa_h \Delta h(p) B_{n,i}\right]} \qquad 22$$

In Equation 22, $\kappa_v = \frac{4\pi}{\lambda}$ and $\kappa_h = \frac{4\pi}{\lambda R \sin\theta}$ group the factors linking velocity to time and height to normal baseline. For the sake of simplicity, we did not include here the flat terrain term: we assume it was already removed. The solution is given by the pair $\Delta\tilde{h}(p)$, $\Delta\tilde{v}(p)$ which maximizes the absolute value of the periodogram

$$\Delta\tilde{v}(p), \Delta\tilde{h}(p) = \arg\max\left\{\left|\xi[\Delta v(p), \Delta h(p)]\right|\right\} \qquad 23$$

The maximum of the absolute value of the periodogram is called temporal coherence

$$\tilde{\xi}(p) = \left|\xi\left[\Delta\tilde{v}(p), \Delta\tilde{h}(p)\right]\right| \qquad 24$$

When the model driven by $\Delta\tilde{h}(p)$, $\Delta\tilde{v}(p)$ matches the observed interferometric phase, the argument of the periodogram in Equation 22 is close to zero, and the temporal coherence tends to 1. Conversely, if the model does not match the observed phase, the argument of the periodogram will be random-like and the temporal coherence will get low values. Very important in this discussion is the number of images N_I used in the estimate. A low number of images will bias the temporal coherence to higher values, making it difficult to distinguish between stable and noisy points.

We are now ready to run the estimation in our test area. Figure 15 shows the PSI module for time series processing. In the left frame we can choose the parameters we want to estimate, and we select height and velocity. The search range of the height is -50m ÷ 150m, while for the velocity -50mm/year ÷ 50mm/year. The result of the analysis is shown in Figure 16. The two upper plots in Figure 16 are the estimated velocity and height, while the lower plot contains the temporal coherence. From Figure 16 we can see that the bottom of the 3 buildings has been processed well, with the model matching the observed phase. In fact, the temporal coherence has values close to 1 and the estimated parameters look reasonable. However, the tops of the buildings have low coherence (around 0.3), and the estimated parameters show unreasonable jumps. To conclude, the analysis was only partly successful. The model we are using to process the InSAR time series of the top of the building is not matching the observations. In the next paragraph, we introduce a model modification to solve the situation.

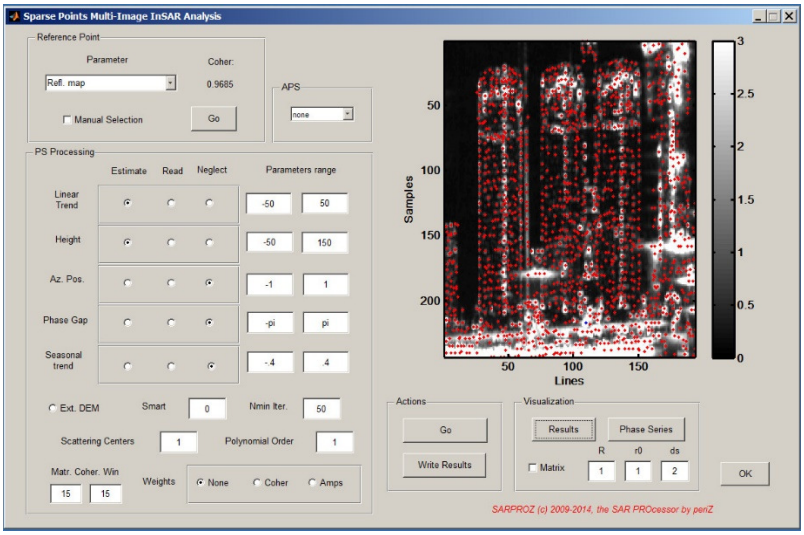

Figure 15. PSI processing module. The settings show that the targets were processed estimating velocity (linear trend) and height. Velocity range: -50 ÷ 50 mm/year. Height: -50 ÷ 150 m.

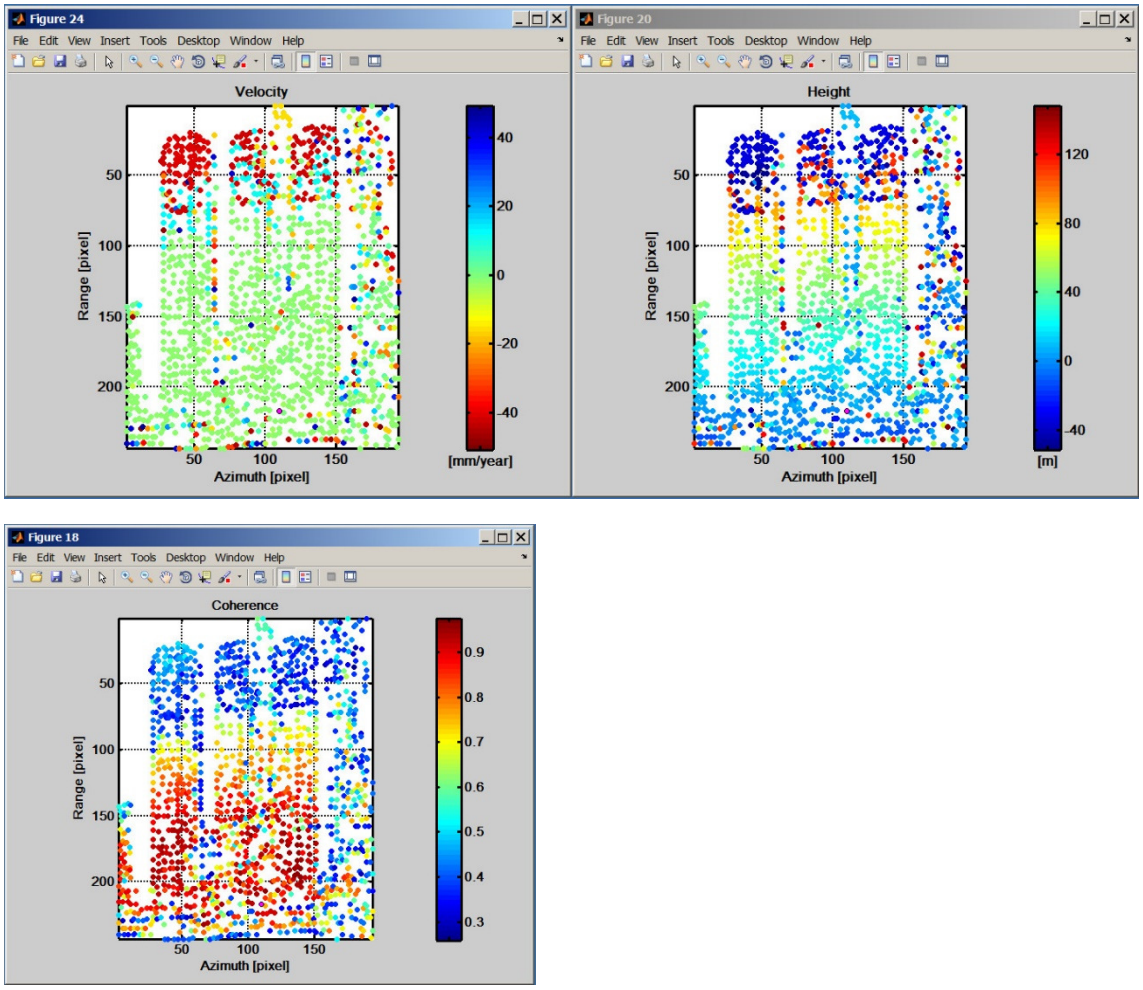

Figure 16. PSI processing results. Upper left corner: estimated velocity. Upper right corner: estimated height. Lower image: estimated coherence. Where the temporal coherence is high (.7÷.9) the estimated parameters are reasonable. For lower coherence values (less than .5) both velocity and height show unreasonable jumps. The model is not matching the data.

Seasonal signals

The reason for the failure of the time series processing described in the previous paragraph is that high buildings suffer thermal expansion [23]. As a consequence, by taking a reference point on the ground, targets at high elevation have a displacement which is not well modeled by a linear trend. The solution has then to be found by introducing a new model which can account for seasonal expansion. In particular, we can expect higher elongations with higher temperature. A possible model is thus the following

$$\Delta\phi_{i,k}^{therm}(p) = \frac{4\pi}{\lambda}\Delta\alpha(p)T_i \qquad 25$$

In Equation *25* T_i is the temperature at the acquisition time[2] and $\Delta\alpha(p)$ is the thermal expansion coefficient of point *p* with respect to the reference point, measured in mm/degC. Equation *25* can be added to the model and the periodogram solved for three unknowns: height, velocity and thermal expansion coefficient.

Figure 17 shows the PSI module with the new added option for including in the estimation also the thermal expansion. Thermal expansion coefficient search values range from -.2 to .6 mm/degC. Figure 18 summarizes the result of the estimation. The first two plots report estimated height and velocity. The lower plots show coherence and thermal expansion coefficient. This time, targets on the buildings are coherent, the estimated velocity shows that no important movement is affecting the buildings, the estimated height is proportional to the buildings profile, and the thermal expansion coefficient is well correlated with the building height. The result demonstrates that the main reason for the low coherence detected on the building was due to the un-modeled thermal expansion.

Several points in Figure 18 still show low coherence values. Such points are not well modeled neither by linear nor by seasonal displacement. In this particular example, the reason for low coherence resides in temporal random changes. The strip of low coherence targets on the right of the first building (starting from the left) is a harbor docking line, where boats stop for short periods of time. The strip of land on the right of the image is an area under construction, with excavators, cranes and other mechanical objects in motion. Thus both areas cannot be analyzed with Multi-Temporal InSAR. In the next paragraphs we will see other possible model extensions to fit different scenarios.

Before moving to other extensions of the PSI technique, we take a look of the geocoded results we've just processed. Figure 19 shows the results of the PSI processing in geographic coordinates over an optical layer as background. Figure 20 displays the same module, but the PSI results are plotted in 3 dimensions, with a color proportional to the estimated thermal expansion coefficient. The list of values beside the picture is relative to a selected point. Values show the target temporal coherence (.72), its height (113m), displacement velocity (0mm/year), thermal expansion coefficient (.35 rad/degC). Finally, Figure 21 displays an example of time series. Figure 21 is divided into two parts: in the upper one, the SAR intensity of the target at hand is plotted versus time; in the second one, the displacement in millimeters is plotted as a function of the acquisition time. In the second plot, 5 replicas of the time series are displayed. Replicas correspond to the phase ambiguity of the system: each vertical sample is equivalent. In particular when data are missing, one should consider the possibility that phase jumps occurred from one replica to

[2] Sarproz automatically downloads Temperature data from historic weather records, however, also independent Temperature data can be imported in the system.

another without being detected. In this example, the phase stability is quite high and phase jumps are not likely to have taken place. The trend in time is not smooth because the recorded temperature is not smooth in time. The blue line shows how well the model fits the data.

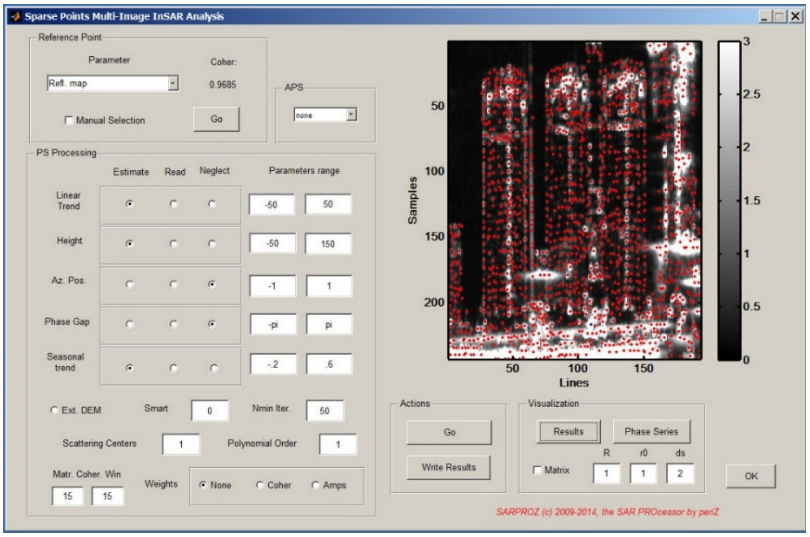

Figure 17. PSI processing module. The settings show that, beside velocity and height, also a seasonal trend is going to be estimated. Range of the thermal expansion coefficient: -.2 ÷ .6 mm/degC

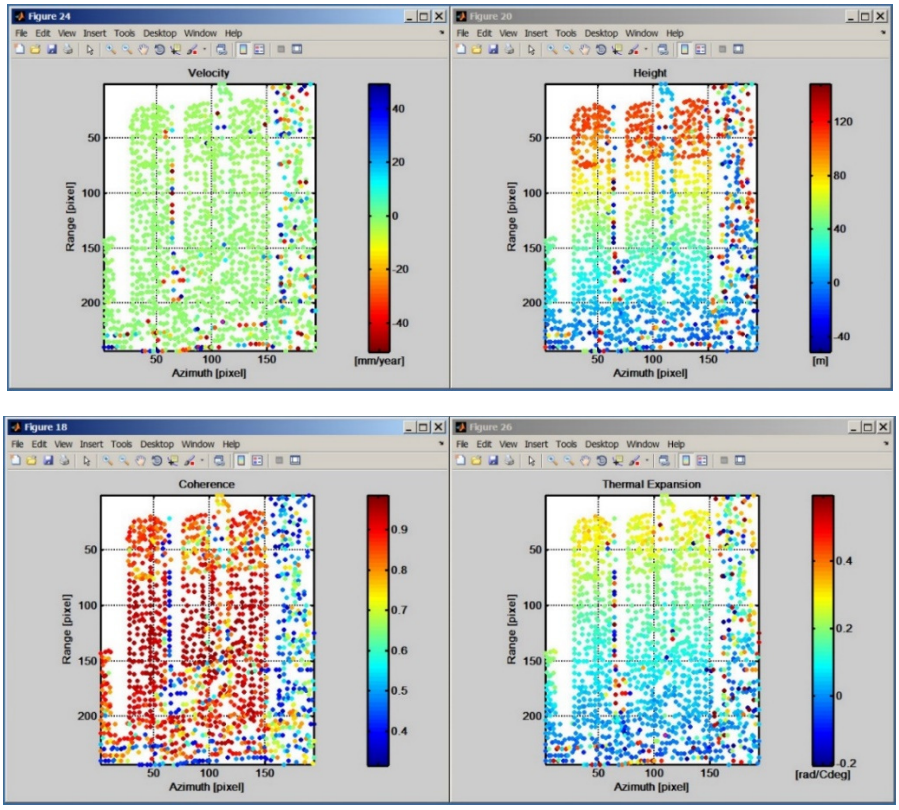

Figure 18. PSI processing results. Upper left corner: estimated velocity. Upper right corner: estimated height. Lower left: temporal coherence. Lower right: thermal expansion. Now the temporal coherence has been increased also for high targets, and all parameters are correctly estimated. The thermal expansion is increasing proportionally to the targets height. Low coherence points are still present on the right of the left building and on the right of the image.

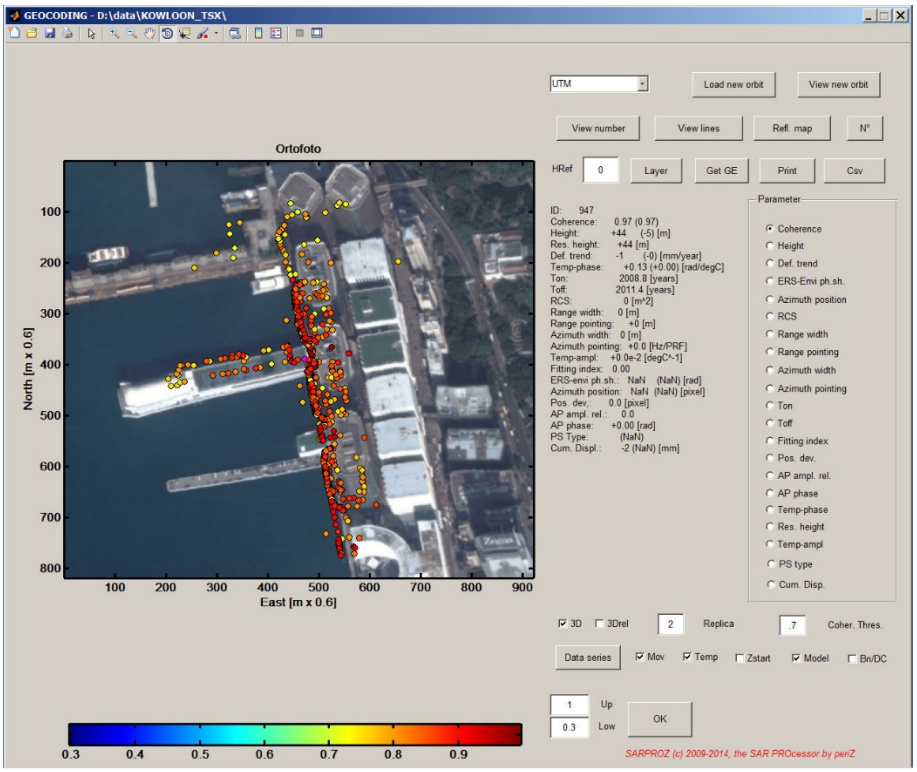

Figure 19. PSI results geocoded on an optical layer. Here the color is proportional to the estimated coherence. One target is selected and a list of estimated parameters is visible on the right of the image.

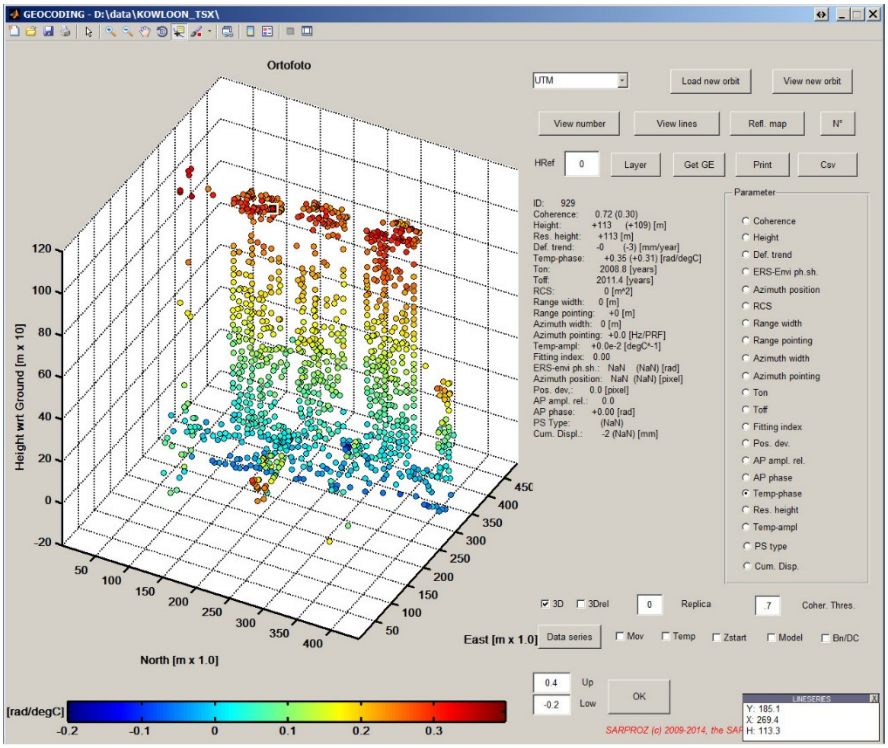

Figure 20. 3D visualization of the geocoded targets. The color is proportional to the thermal expansion coefficient. The three analyzed buildings are well resolved and the targets on the facades are geocoded vertically.

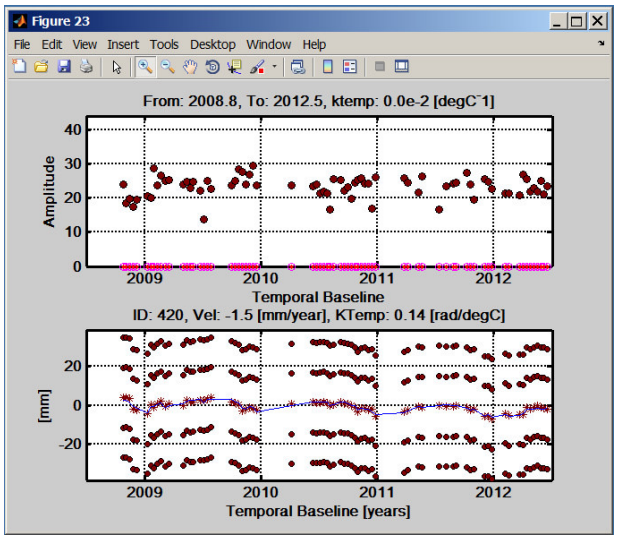

Figure 21. Example of displacement time series. The time trend is not very smooth and not very sinusoidal, because summer in Hong Kong is longer than winter.

Non-linear signals

Low temporal coherence can be caused also by displacement trends which are not linear and not correlated with temperature either. Movements may present acceleration: in this case a good model to use is the polynomial approximation

$$\Delta\phi_{i,k}^{disp}(p) = \frac{4\pi}{\lambda}\Delta v(p)B_{t,i} + \Delta a(p)B_{t,i}^2 \qquad 26$$

In equation 26, $\Delta a(p)$ is the acceleration of point *p* with respect to the reference. Other possible temporal behaviors are multiple linear segments, sudden jumps (like in the case of landslides activation or earthquakes), seasonal patterns (but not related to temperature, like dam oscillations related to the water level) or a combination of more of them. Even if still keeping the model-approach for comparison and for educational purposes, Sarproz is now including alternative ways to process time series, without the need of models. An example is reported in Figure 22. A dam in Hong Kong has been analyzed without displacement models, and a time series is reported on the left. The time series is displaying the interferometric phase after removal of the geometric terms (no smoothing is applied). The blue line, conversely, is derived by smoothing the phase to follow the displacement trend avoiding possible noisy oscillations. In the example in Figure 22 the noise level is very low and smoothed line and phase values match pretty well.

When non-linear displacement trends are analyzed, velocity maps are not meaningful anymore. Cumulative displacement maps should be considered instead. A cumulative displacement map shows the total amount of millimeters a given area on the ground moved from the beginning to the end of the analyzed period. An example is shown in Figure 23. A dataset of 64 TerraSAR-X images has been processed in Los Angeles. Red areas show a cumulative displacement of -50mm in the period 2010-2014. Red spots in the picture identifies oil extraction areas. One of them has also blue features, meaning that water or gas is pumped underground to stabilize the subsidence. The Los Angeles basin is known to be characterized by seasonal movements. A linear analysis here would never work.

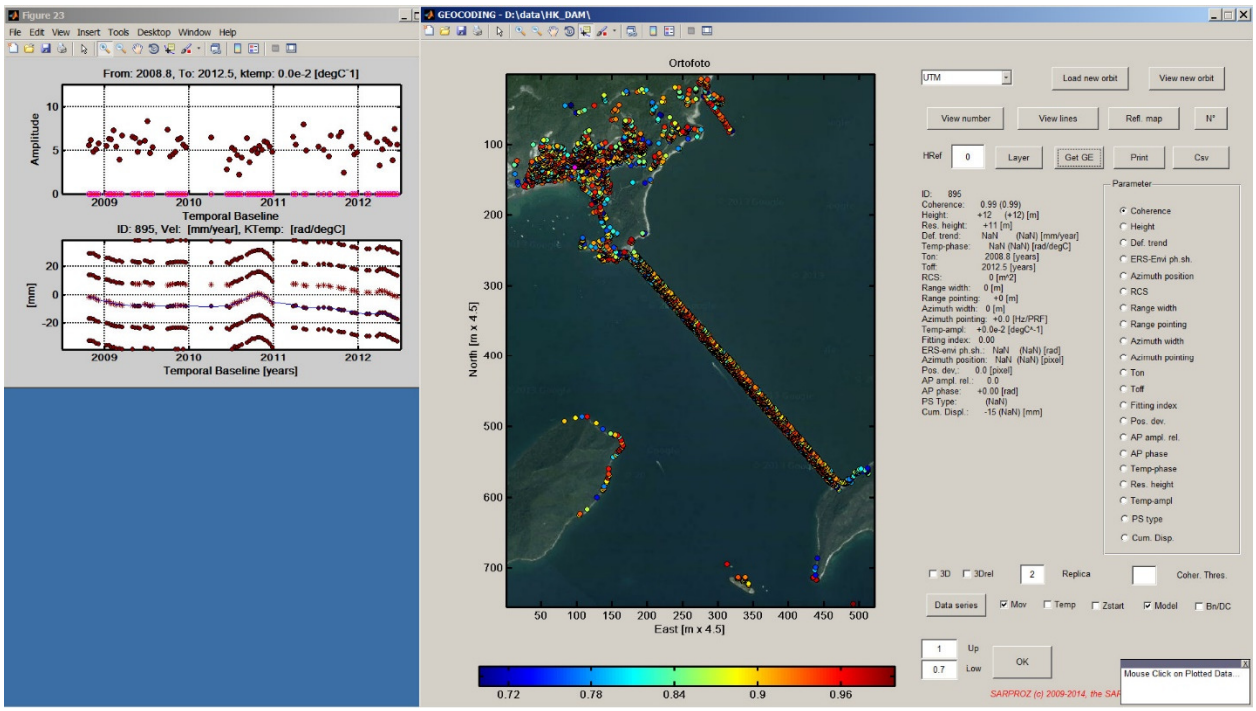

Figure 22. A dam in Hong Kong. On the right: targets detected on the Dam structure. On the left: non-linear time series detected by Sarproz. Notice that the software does not apply any smoothing operation: the phase displayed there is the original interferometric phase after removing the topographic term.

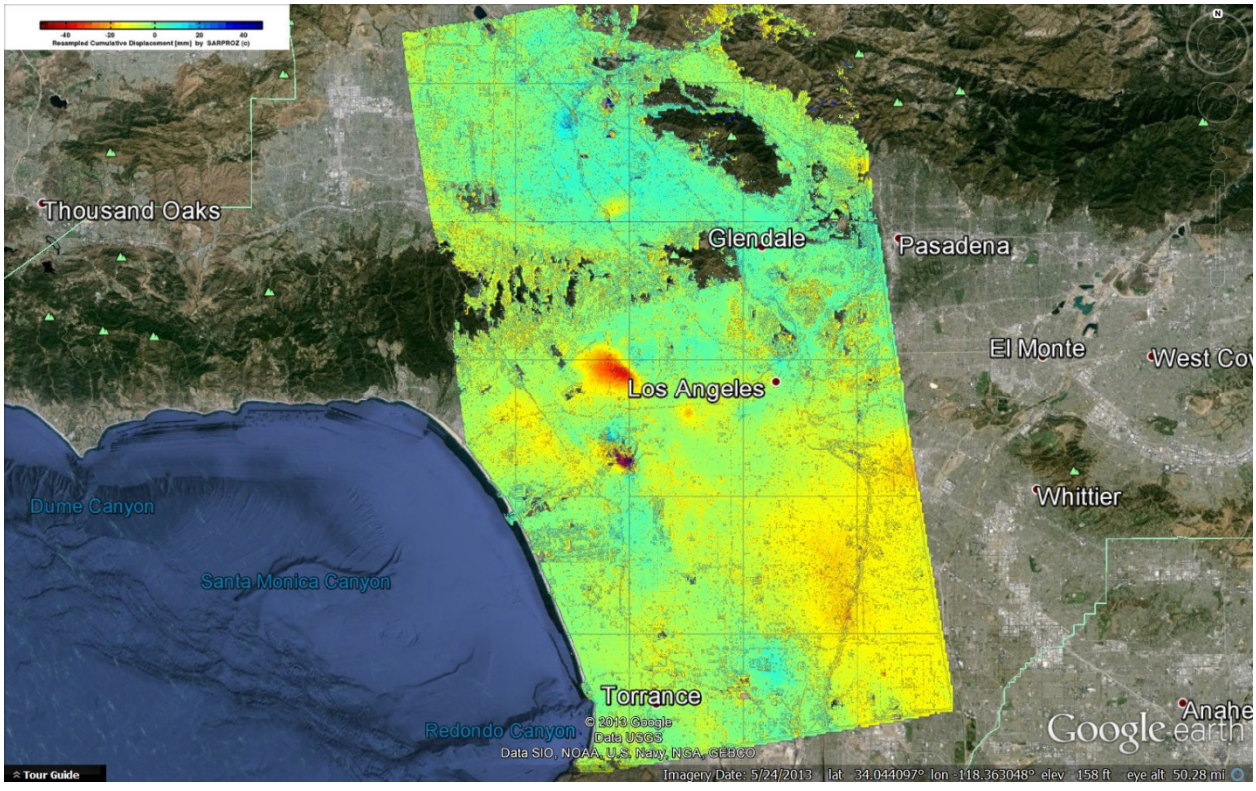

Figure 23. Cumulative displacement map detected by Sarproz in Los Angeles using 64 TerraSAR-X images. Red corresponds to about -50mm, in the period 2010-2014. The two spots of subsidence are over Oil extraction fields.

The multi-master approach

PSI techniques solved the main InSAR issues and made it possible to retrieve reliable time series from archived SAR data. However, the original PSI concept as published in [5] is very restrictive. In fact, according to the primordial algorithm, a target is required to be coherent in all interferograms generated with a single Master image. Such a strong condition is met only by manmade isolated targets whose dimensions are much smaller than the resolution cell. Whilst urban areas usually are characterized by such features, it is very difficult to find them in other scenarios (as rural/deserted/mountainous areas). The need thus for increasing the density of coherent targets also in extra-urban areas brought to a series of improvements/generalizations of the original PSI algorithm. We already mentioned in the introduction a couple of them (SBAS, StamPS and Squeesar), we briefly describe here the algorithm implemented by Sarproz: the Quasi-PS technique [28].

The main idea of multi-master approaches is to relax the strict conditions imposed by PSI techniques. Thus, instead of analyzing the InSAR phase generated with respect to a single Master image, more options can be considered. If the computational power is not an issue, all possible interferograms should be evaluated, searching for the coherent ones. Otherwise, subset of interferograms can be selected (as small normal baseline subsets or pairs that can guarantee the connectivity of the images graph [28]). In any case, in a multi-master framework, in Equation *19* and following, index *k* does not refer any more to a single image. Moreover, in the single-master approach, the number of samples per equation in the periodogram (Equation *22*) was indicated as N_I (equal to the number of images and also to the number of interferograms[3]). In a multi-master approach, the number of samples of Equation *22* is equal to the number of interferograms N_{Int}, which is usually higher than N_I. By taking into account these points, we can modify Equation *22* in the following way:

$$\xi[\Delta v(p),\Delta h(p)]=\frac{1}{N_{Int}}\sum_{i,k}^{N_{Int}} e^{j\left[\Delta\phi_{i,k}(p)-\kappa_v\Delta v(p)B_{t,i,k}-\kappa_h\Delta h(p)B_{n,i,k}\right]} \qquad 27$$

In Equation *27*, the sum is carried out on N_{Int} *i,k* pairs. Similarly to the single-master case, we can solve the system by searching for the model parameters (velocity and height in Equation *27*) which maximize the absolute value of the periodogram.

Figure 24 shows an example of DEM estimation by means of a Quasi-PS analysis of ALOS data. The image on the left of Figure 24 is the interferometric combination used in the analysis: 34 interferograms were generated out of 9 images. The image on the right shows the estimated height in Google Earth. No initial DEM was removed from the interferometric phase and no initial phase unwrapping was applied. This analysis shows that Multi-Temporal InSAR can provide a more reliable phase unwrapping than working with single interferograms.

Weighted approaches

Together with the multi-master idea, a big improvement with respect to the original PSI algorithm is the introduction of weights in the parameters estimation. Weights act as flags that tell us in which interferograms a given target is coherent. Thus, not only highly coherent targets (Persistent Scatterers)

[3] Here for the sake of simplicity we assume that an all-zeros interferogram (Master-Master) is included in the dataset.

can be successfully processed, but also decorrelating targets, thanks to the adaptive choice of interferograms subsets. For instance, seasonal targets (as mountain tops periodically covered by snow or trees loosing leaves) may be coherent only in summer (or only in winter) months. Extended geometrically decorrelating targets (as fields, low density vegetation) may be coherent only in very short normal baselines. Temporally decorrelating targets (as growing vegetation, areas under construction), may be coherent only in short temporal baselines. By knowing in which interferograms each of those target typologies is coherent, we can mask uncoherent interferograms out and keep only the informative ones.

The utilization of weights can be implemented with just a small modification in Equation *27*. In order to keep an InSAR phase sample in the height/velocity estimation (or in order to disregard it) we can insert the weight $w_{i,k}$ (a number between 0 and 1) as it follows:

$$\xi[\Delta v(p),\Delta h(p)]=\frac{1}{\sum w_{i,k}}\sum_{i,k}^{N_{Int}} w_{i,k}e^{j\left[\Delta\phi_{i,k}(p)-\kappa_v\Delta v(p)B_{t,i,k}-\kappa_h\Delta h(p)B_{n,i,k}\right]} \qquad 28$$

The process for estimating the model parameters is still the same, but only InSAR pairs with high weight $w_{i,k}$ will be used. Notice that the same modification could be applied in a single-master framework with the same effect.

The Quasi-PS algorithm uses the absolute value of the interferometric coherence $\gamma_{i,k}(p)$ in Equation *17* as weight. Sarproz gives different options for the choice of weights. Besides the coherence, another option is using intensity values or models estimated by processing intensity values. This is particularly useful when dealing with areas under construction, where targets remain coherent for short periods of time.

An example of a temporary target is reported in Figure 25. The upper plot on the left in Figure 25 displays the radar signal intensity, showing that the target disappeared in 2010. The plot below shows the displacement time series. Without masking the data-series for the life-time of the target, it would not be possible to successfully process it.

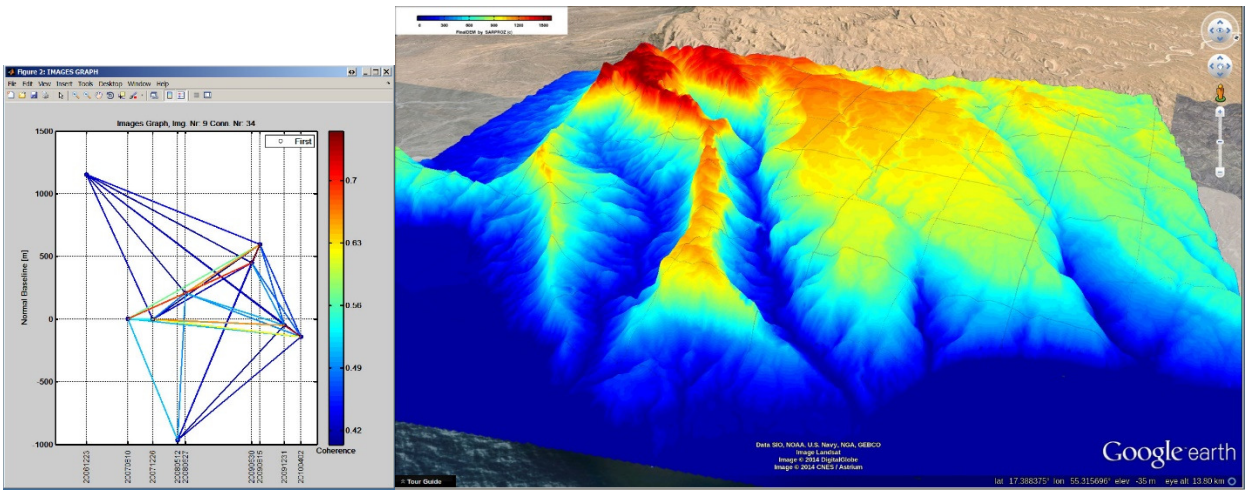

Figure 24. Example of DEM generated via Quasi-PS analysis. On the left, interferometric configuration: 34 interferograms were generated out of 9 ALOS images. On the right, estimated height. Notice that no DEM was removed from the interferograms for this purpose. Multi-Temporal InSAR performs a reliable phase unwrapping.

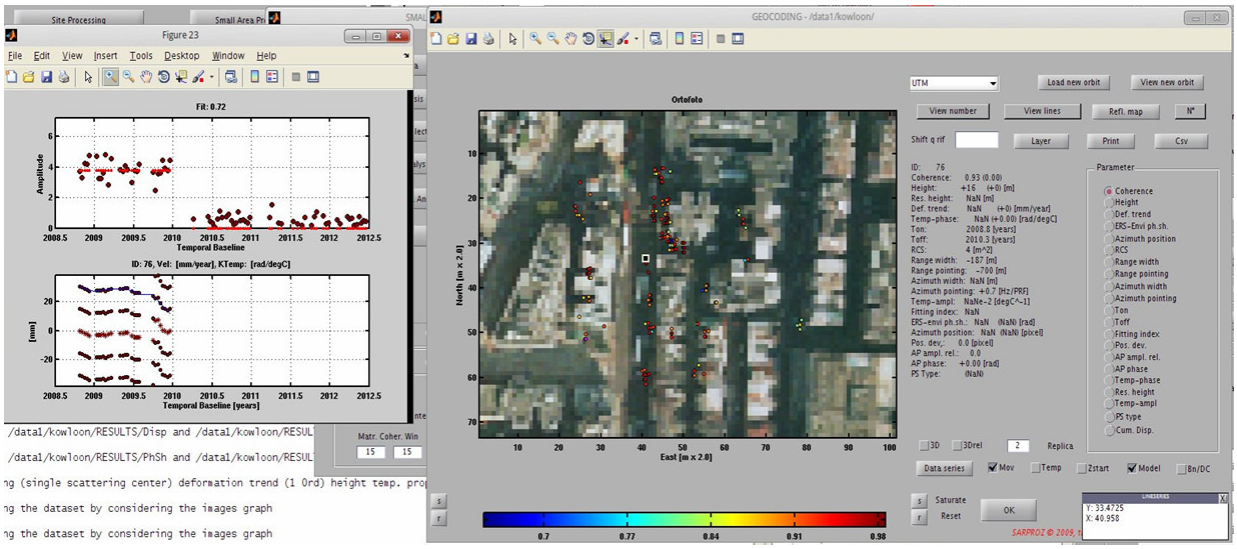

Figure 25. Example of temporary target in Hong Kong. The plot on the left, upper position, shows the intensity as a function of time. It is easy to observe that the target at hand was visible for a short period of time. The plot below shows the displacement time series during the target life time.

Conclusions

In this Chapter we have discussed the basic theory behind SAR interferometry and Multi-Temporal InSAR. In particular, we have seen that InSAR is potentially a very powerful technology to estimate DEMs and ground movement, but also that InSAR is affected by important limitations (as decorrelation, phase ambiguity and atmospheric biases). Multi-Temporal InSAR techniques offer a series of tools for attenuating InSAR limitations, making it possible to process and analyze displacement time series, and also to precisely estimate ground elevation.

References

[1] Graham, L. C., "Synthetic Interferometer Radar for Topographic Mapping," Proc. of the IEEE, 62(2), 763-768,1974.

[2] Goldstein, R. M., H. A. Zebker, and C. L. Werner, "Satellite Radar Interferometry: Two-Dimensional Phase Unwrapping," Radio Science, 23(4), 713-720, 1988.

[3] Zebker, H. A. and J. Villasenor, "Decorrelation in Interferometric Radar Echoes", IEEE Trans. on Geosci. and Remote Sens., 30(5), 950-959, 1992.

[4] Hanssen, Ramon F. (2001), Radar Interferometry: Data Interpretation and Error Analysis, Kluwer Academic, ISBN 9780792369455.

[5] A. Ferretti, C. Prati, and F. Rocca, "Permanent scatterers in SAR interferometry," IEEE Trans. Geosci. Remote Sens., vol. 39, no. 1, pp. 8–20, Jan. 2001.

[6] P. Berardino, G. Fornaro, R. Lanari, and E. Sansosti, "A new algorithm for surface deformation monitoring based on small baseline differential SAR interferograms," IEEE Trans. Geosci. Remote Sens., vol. 40, no. 11, pp. 2375–2383, Nov. 2002.

[7] A. Hooper, H. Zebker, P. Segall, and B. Kampes, "A new method for measuring deformation on volcanoes and other natural terrains using InSAR persistent scatterers," Geophys. Res. Lett., vol. 31, p. L23 611, 2004.

[8] Ferretti, A., Fumagalli, A., Novali, F., Prati, C., Rocca, F. & Rucci, A., 2011. A New Algorithm for Processing Interferometric Data - Stacks: SqueeSAR. IEEE TGRS, vol. 49, no. 9, p. 3460.

[9] Moreira, A. Prats-Iraola, P. ; Younis, M. ; Krieger, G. ; Hajnsek, I. ; Papathanassiou, K.P., "A tutorial on synthetic aperture radar", Geoscience and Remote Sensing Magazine, IEEE (Volume:1 , Issue: 1), March 2013.

[10] Zhong Lu, Lei Zhang, "Frontiers of Radar Remote Sensing", PE&RS, January 2014.

[11] C. Colesanti, J. Wasowski, "Investigating landslides with space-borne synthetic aperture radar (SAR) interferometry" Engineering Geology, 88 (3–4) (2006), pp. 173–199.

[12] Herrera, G.; Tomás, R.; Vicente, F.; Lopez-Sanchez, J.M.; Mallorquí, J.J.; Mulas, J. (October 2010). "Mapping ground movements in open pit mining areas using differential SAR interferometry". International Journal of Rock Mechanics and Mining Sciences 47 (7): 1114–1125.

[13] Massonnet, D.; Rossi, M.; Carmona, C.; Adragna, F.; Peltzer, G.; Feigl, K.; Rabaute, T. (1993), "The displacement field of the Landers earthquake mapped by radar interferometry", Nature 364 (6433): 138–142

[14] Wadge, G. (2003), "A strategy for the observation of volcanism on Earth from space", *Phil. Trans. Royal Soc.Lond.* **361**: 145–156

[15] A Ferretti, C Prati, F Rocca, "Multibaseline InSAR DEM reconstruction: The wavelet approach", IEEE Transactions on Geoscience and Remote Sensing, 37 I. 2, Mar 1999

[16] M. Martone, P. Rizzoli, B. Bräutigam and G. Krieger, "First 2 years of TanDEM-X mission: Interferometric performance overview", Radio Science Volume 48, Issue 5, pages 617–627, September-October 2013

[17] M.E. Engdahl, J.M. Hyyppa "Land-cover classification using multitemporal ERS-1/2 InSAR data" IEEE Transactions on Geoscience and Remote Sensing 08/2003.

[18] J. C. Curlander and R. N. McDonough, Synthetic Aperture Radar: Systems and Signal Processing. New York: Wiley, 1991.

[19] A. Ferretti, A. Monti-Guarnieri, C. Prati, F. Rocca "InSAR Principles: Guidelines for SAR Interferometry Processing and Interpretation" (TM-19, February 2007).

[20] Kampes, Bert M. Radar interferometry: persistent scatterer technique. Vol. 12. Springer, 2006.
[21] D. Perissin, Sarproz webpage www.sarproz.com
[22] D. Perissin, Z.Wang, and T.Wang, “The SARPROZ InSAR tool for urban subsidence/manmade structure stability monitoring in China,” in Proc. 34th Int. Symp. Remote Sens. Environ. (ISRSE), Syndey, Australia, Jan. 2011.
[23] D. Perissin and F. Rocca, “High accuracy urban DEM using permanent scatterers,” IEEE Trans. Geosci. Remote Sens., vol. 44, no. 11, pp. 3338–3347, Nov. 2006.
[24] D. Perissin, C. Prati, M. Engdahl, and Y. L. Desnos, “Validating the SAR wavenumber shift principle with the ERS–Envisat PS coherent combination,” IEEE Trans. Geosci. Remote Sens., vol. 44, no. 9, pp. 2343–2351, Sep. 2006.
[25] R. M. Goldstein and C. L. Werner, “Radar interferogram filtering for geophysical applications,” Geophys. Res. Lett., vol. 25, no. 21, pp. 4035–4038, Nov. 1998.
[26] I. Baran, M. P. Stewart, B. M. Kampes, Z. Perski, and P. Lilly, “A modification to the Goldstein radar interferogram filter,” IEEE Trans. Geosci. Remote Sens., vol. 41, no. 9, pp. 2114–2118, Sep. 2003.
[27] Z Li, JP Muller, P Cross, EJ Fielding, "Interferometric synthetic aperture radar (InSAR) atmospheric correction: GPS, Moderate Resolution Imaging Spectroradiometer (MODIS), and InSAR integration", Journal of Geophysical Research: Solid Earth (1978–2012) 110 (B3)
[28] Perissin, D. & Wang, T. (2012). Repeat-Pass SAR Interferometry with Partially Coherent Targets. IEEE T. Geoscience and Remote Sensing, 50, 271-280.